energies

Article

Study on Flow and Heat Transfer Characteristics of 25 kW Flameless Combustion in a Cylindrical Heat Exchanger for a Reforming Processor

Ruiqi Zhu [1] and Donghoon Shin [2,*]

[1] Department of Mechanical Engineering, Kookmin University, Seoul 02707, Republic of Korea; zurrachi@foxmail.com
[2] School of Mechanical Engineering, Kookmin University, Seoul 02707, Republic of Korea
* Correspondence: d.shin@kookmin.ac.kr

Abstract: Flameless combustion has advantages such as low pollution and uniform temperature in the combustion chamber, making it an excellent option for heat exchangers. Previous studies have focused solely on the flameless combustion phenomenon, without considering its interaction with the target being heated. In this study, we conducted experimental and computational fluid analyses on a cylindrical reformer for reverse air injection flameless combustion. Typically, small-scale reformers of 10 kW or less are coaxial triple-tube cylindrical reformers. In contrast, multitubular reformers are used for larger-scale applications, since the heat transfer rate in single-burner cylindrical reformers decreases sharply as the scale increases. Flameless combustion, with high heat transfer efficiency, helps overcome the limitation of premixed burner. Compared with conventional premixed burners, flameless burner decreases the combustion gas outlet temperature by 30% at 25 kW while reducing energy consumption by 24% (owing to the high heat transfer rate) for a given cooling fluid outlet temperature. Furthermore, it is shown that introducing a ring at the combustion chamber exit can enhance combustion gas recirculation. The experimental result was confirmed through computational fluid analysis. It is concluded that for reverse air injection flameless combustion, the combustion gas recirculation rate in the combustion chamber is strongly related to the heat transfer.

Keywords: flameless combustion; reverse air injection; cylindrical heat exchanger; heat transfer efficiency; computational fluid dynamics; hydrogen reformer

Citation: Zhu, R.; Shin, D. Study on Flow and Heat Transfer Characteristics of 25 kW Flameless Combustion in a Cylindrical Heat Exchanger for a Reforming Processor. *Energies* **2023**, *16*, 7160. https://doi.org/10.3390/en16207160

Academic Editor: Artur Blaszczuk

Received: 2 August 2023
Revised: 27 September 2023
Accepted: 27 September 2023
Published: 19 October 2023

1. Introduction

Hydrogen energy is a promising next-generation energy resource, as it is a clean and sustainable alternative to fossil fuels for various applications, such as transportation and power generation [1]. Proton-exchange membrane fuel cells have been widely researched and developed, since they are environmentally friendly and have high energy conversion efficiency [2]. They are expected to help address climate change and promote the transition to a more sustainable energy landscape. In fuel cell operation, the reforming process is a critical step, as it converts hydrocarbon fuels into hydrogen-rich gas [3]. To achieve better performance, extensive research is being conducted on methods to enhance efficiency, reduce emissions, and produce energy from alternatives to fossil fuels [4].

Reforming reactions generally occur at temperatures above 700 °C, at which the heat generated by combustion in heat exchangers causes steam and hydrocarbons to undergo catalytic reactions to produce hydrogen [5]. Therefore, the effective control of heat transfer and enhancing the durability and safety of the heat exchanger of a reformer at high temperatures are important research directions [6].

In this study, a flameless combustion technique called reverse air injection (RAI) was used [7–9]. RAI maximizes the delay of meeting of air and fuel by injecting air and fuel in opposite directions in the combustion chamber. The high recirculation rate of combustion gases in the combustion chamber reduces the fuel and oxidizer concentrations immediately due to mixing with the recirculating gas, resulting in a finely dispersed combustion. This ensures a uniform temperature distribution and increases the efficiency of heat transfer to the heat exchanger surface [10]. Previous research has focused solely on the flameless combustion phenomenon, without considering its interaction with the target to be heated, since flameless combustion has an instability problem at low temperatures under 800 °C [11–13].

In the selection of a computational fluid dynamics (CFD) simulation model for RAI flameless combustion, an improved k-ε model with modified parameters was employed in the Reynolds-averaged Navier–Stokes (RANS) turbulence model to solve the time-averaged equations of fluid motion [14]. As the radiation model, which plays a crucial role in the analysis of the overall heat transfer and temperature distribution in the flameless combustion zone, an accurate but computationally demanding discrete-ordinates (DO) model was employed. This model discretizes the angular domain into a finite number of directions to solve the radiative transfer equation [15].

The choice of an accurate species model is crucial for predicting species concentrations, reaction rates, and pollutant emissions in flameless combustion. For operation in the flameless combustion regime, where there is spread of elevated temperature and reduced oxygen levels, the reaction rates are reduced, and the effect of molecular diffusion on flame properties is large. The eddy dissipation concept (EDC) species model, which is widely used for analysis of coflow flameless combustion, has several limitations when used for simulation of the RAI method, owing to the reaction rates being limited by the turbulence dissipation rates, simplified chemical reaction mechanisms, and the inability to accurately capture downstream strain and dilution effects [16]. We attempted to use the equilibrium probability distribution function (PDF) model and composition PDF model [17–20] (also called the transport PDF model) instead of the commonly used EDC model to predict the species reaction mechanisms in RAI flameless combustion, with the objective of identifying the reasons and mechanisms underlying species reactions by comparing experimental and CFD results [21].

As feedstock for the reformer, in this study, we considered an ethanol–water mixture instead of a methane–steam mixture. The advantages of this choice include its renewability, lower carbon dioxide emissions, milder reaction conditions, higher hydrogen production rates, reduced risk of carbon deposition, and better compatibility with small-scale distributed power generation systems [22,23]. With the increasing demand for clean and sustainable energy, ethanol steam reforming may play a significant role in hydrogen production for various applications, such as fuel cells, transportation, and power generation [24]. However, in this study, water was used instead of ethanol to determine the heat transfer efficiency by measuring the heat transfer rate accurately with water evaporation phenomena to improve the efficiency of the reformer and to reduce environmental pollution. Insights into and perspectives on the design of a coaxial cylindrical reformer are provided on the basis of experimental and simulation results, as well as on the basis of the theory of flameless combustion.

2. Research Methods

2.1. Experiment

2.1.1. Experimental Equipment and Design

Figure 1 shows a schematic diagram of a 25 kW reformer. A porous plate-type premixed burner is located at the bottom center. For flameless combustion, two high-speed combustion air jets (>100 m/s) are injected upward from nozzles positioned at one-quarter of the combustion chamber diameter at the bottom of the combustion area, while fuel is vertically injected downward from the top center. Combustion gases recirculate within the combustion chamber before being discharged at the bottom of the combustion chamber. The cylindrical combustion chamber is surrounded by a coaxial triple-tube reformer used for catalytic reactions. The raw gas enters from the top of the reformer, then returns to the top through the bottom porous plate into the inner side catalyst zone, eventually leaving after passing through the catalyst ($Ni-Al_2O_3$) layer. The outermost and top insulation prevent the overheating of the experimental apparatus, thereby enhancing the safety of the experiment.

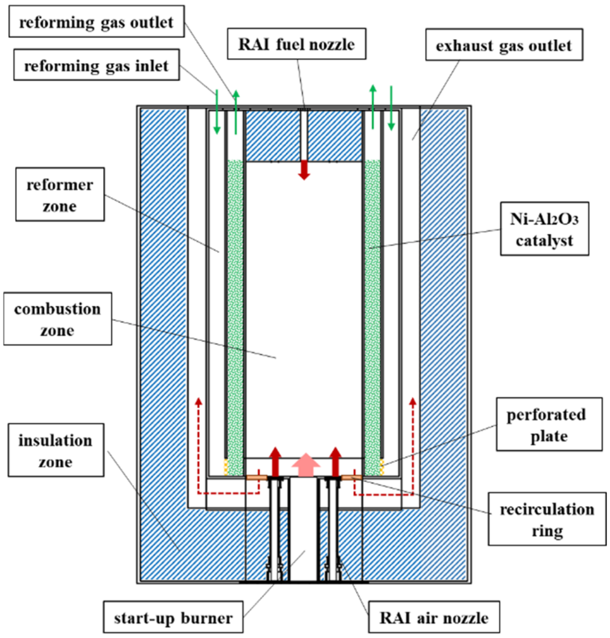

Figure 1. Configuration of the 25 kW coaxial reformer.

Figures 2 and 3 show the geometric dimensions of the 25 kW hydrogen reformer and the locations of internal thermocouples. The T.C.@1 and T.C.@2 thermocouples in the combustion zone were positioned at the top and bottom, respectively, and the outlet temperature of the catalyst layer was measured by T.C.@3. The temperature at the exhaust gas outlet of the combustion zone was measured by four T.C.@4 thermocouples located peripherally, and the measurements were averaged. T.C.@5, which measured the temperature of the outer wall of the reformer, was positioned at the center height of the reformer.

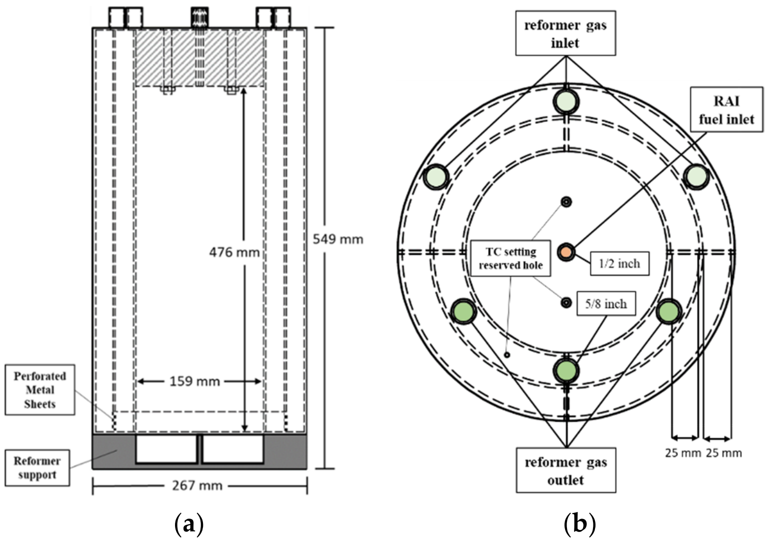

Figure 2. Schematic diagram showing the tubular reformer's geometry. (**a**) Vertical cross section; (**b**) top surface.

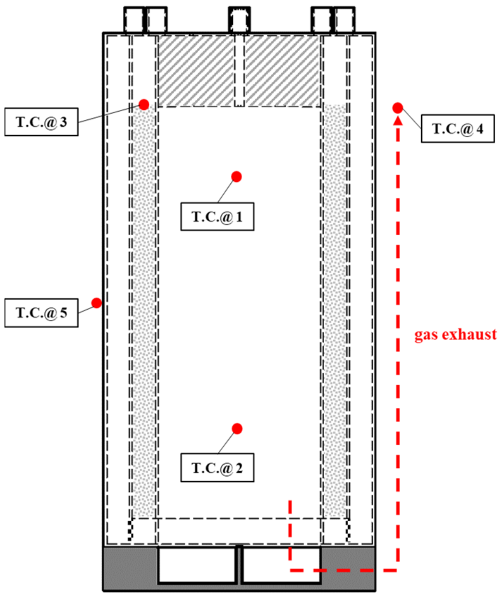

Figure 3. Positions of temperature measurement.

Figure 4 shows the configuration of the burner, which includes a permeable ignition burner and a pair of air nozzles designed for RAI flameless combustion. The internal diameter of the air nozzles was 7 mm.

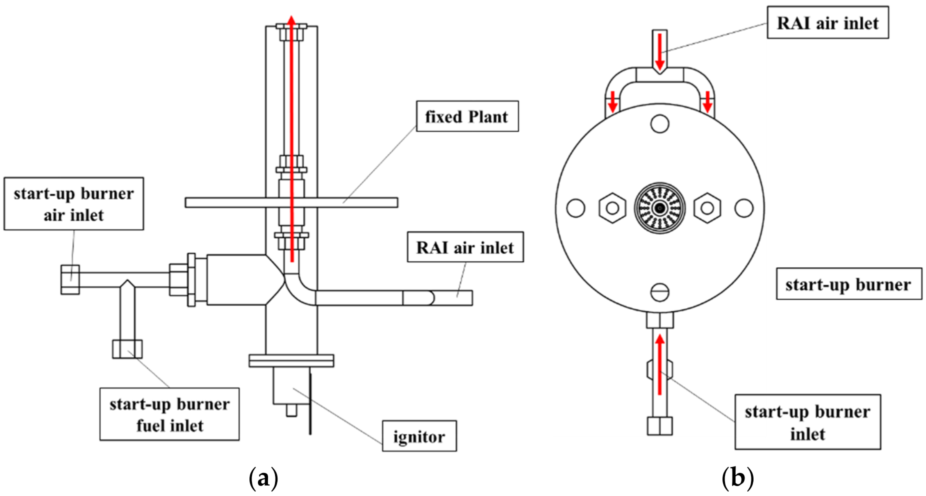

Figure 4. Startup and flameless burner configurations. (**a**) Vertical cross section; (**b**) top view.

Figure 5 shows a schematic diagram of the entire 25 kW reforming experimental apparatus. Mass flow regulators (Bronkhorst Inc., Ruurlo, The Netherlands) were employed to regulate the flow of air (F-202AV: max flow = 250 L/min, precision = ±0.5%) and fuel (F-201CV: max flow = 25 L/min, precision = ±0.5%). The catalyst zone was heated by the premixed burner, and after the temperature of the reformer and the average temperature of the combustion chamber reached 600 °C and 800 °C, respectively, the three-way valves of air and fuel were switched to generate RAI flameless combustion. During the experiment, temperature data of the reformer were collected under various experimental conditions in the steady state using a Yokogawa MV2000 DAQ system; bare-bead K-type thermocouples (ϕ1 mm, T_{max} = 1360 °C, precision: ±1 °C) were used to minimize environmental interference. Testo 330 LL (resolution: O_2 = 0.1%, CO = 1 ppm, NO = 1 ppm) was employed to monitor the concentrations of oxygen, carbon monoxide, and nitrogen oxides generated during combustion.

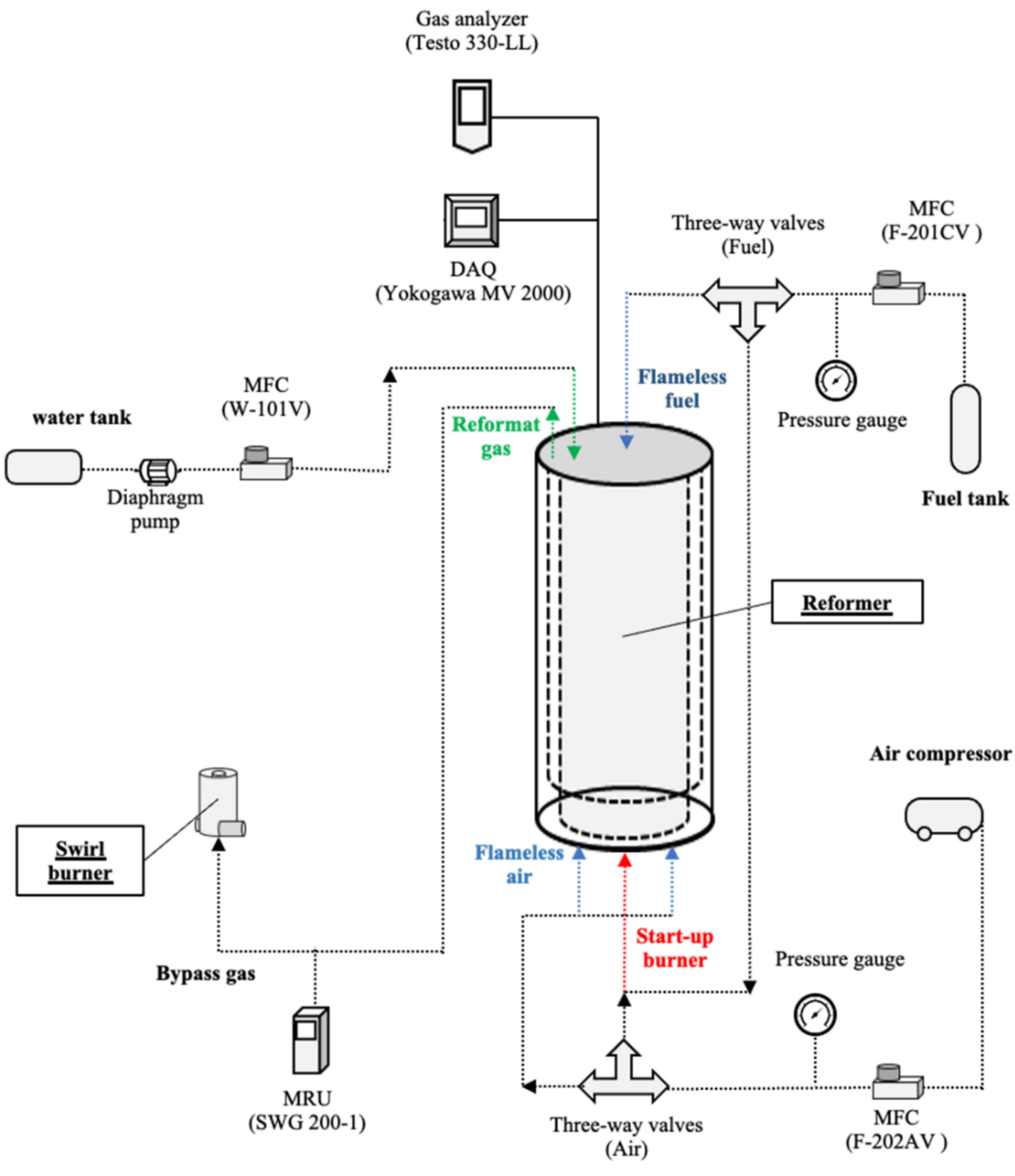

Figure 5. Schematic diagram of the experimental setup.

2.1.2. Experimental Conditions

To analyze the heat transfer characteristics of the 25 kW RAI flameless combustion system, we first examined the results of previous experiments conducted with a 5 kW cylindrical flameless combustor [25]. In the experiment's design and innovation, a recirculation ring (shown in Figure 1) was added to the outer side of the air nozzle of the burner for comparison of heat transfer rate and NO emissions, with the aim of increasing the recirculation rate within the combustion chamber and the heat transfer efficiency of the reformer. The combustion modes and RAI configurations were categorized into three groups, as outlined in Table 1. Groups A and B comprised instances of RAI flameless combustion, differing by the presence or absence of a recirculation ring, and group C represented a premixed combustion condition.

Table 1. Operation conditions.

	Heat Input	Fuel Flow	Air Flow	Water Flow	Fuel Nozzle Diameter	Air Nozzle Diameter	Fuel Flow Velocity	Air Flow Velocity
	(kW)	(L/min)	(L/min)	(cc/min)	(mm)	(mm)	(m/s)	(m/s)
Group A—RAI flameless								
A-1	15.4	10	300	18	7	6	4.3	88.4
A-2	24.6	16	480	29			6.9	141.5
A-3	33.8	22	660	41			9.5	194.5
Group B—RAI flameless (with recirculation ring)								
B-1	15.4	10	300	18	7	6	4.3	88.4
B-2	24.6	16	480	30			6.9	141.5
B-3	33.8	22	660	41			9.5	194.5
Group C—Premixed flame					Burner diameter (mm)		Burner flow velocity (m/s)	
C-1	15.4	10	300	15	38.9		8.9	
C-2	24.6	16	480	26			19.5	
C-3	33.8	22	660	37			26.8	

2.2. CFD Simulation

2.2.1. CFD Models

In this research, ANSYS Fluent v.18.2 was employed to simulate experimental scenarios for comparative analysis. The model equations used for CFD calculations are presented in Table 2. The turbulence model adopted was the standard k-ε model, which is suitable for circular-hole planar jets [26]. To estimate the radiation heat transfer between the furnace wall, flue gas, and cooling pipe, we used the DO model with a finite number of solid angles, with both theta and phi divisions being set to 10 [27]. Additionally, the weighted sum of the gray gas model was used to calculate the radiation transfer model.

Table 2. Equations to be solved for computational fluid dynamics.

Continuity equation	$\frac{\partial\rho}{\partial t} + \nabla\cdot(\rho u) = 0$	(1)
Momentum Conservation Equation	$\frac{\partial}{\partial t}\left(\rho\vec{v}\right) + \nabla\cdot\left(\rho\vec{v}\vec{v}\right) = -\nabla p + \nabla\cdot\left(\tau\right) + \rho\vec{g} + \vec{F}$	(2)
Turbulent kinetic energy k	$\frac{\partial(\rho k)}{\partial t} + \frac{\partial(\rho k u_i)}{\partial x_i} = \frac{\partial}{\partial x_j}\left[\frac{\mu_t}{\sigma_k}\frac{\partial k}{\partial x_j}\right] + 2\mu_t E_{ij} E_{ij} - \rho\varepsilon$	(3)
Dissipation ε	$\frac{\partial(\rho k)}{\partial t} + \frac{\partial(\rho \varepsilon u_i)}{\partial x_i} = \frac{\partial}{\partial x_j}\left[\frac{\mu_t}{\sigma_\varepsilon}\frac{\partial \varepsilon}{\partial x_j}\right] + C_{1\varepsilon}\frac{\varepsilon}{k}2\mu_t E_{ij} E_{ij} - C_{2\varepsilon}\rho\frac{\varepsilon^2}{k}$	(4)
Energy equation	$\frac{\partial}{\partial t}(\rho H) + \nabla\cdot\left(\rho\vec{v}H\right) = \nabla\cdot\left(\frac{k_t}{c_p}\nabla H\right) + S_h$	(5)
Discrete Ordinates (DO) Radiation model	$\nabla\left(I\left(\vec{r},\vec{s}\right)\vec{s}\right) + (a+\sigma_s)I\left(\vec{r},\vec{s}\right) = an^2\frac{\sigma T^4}{\pi} + \frac{\sigma_s}{4\pi}\int_0^{4\pi} I\left(\vec{r},\vec{s}\right)\Phi\left(\vec{s},\vec{s}'\right)d\Omega'$	(6)
Species transport	$\frac{\partial}{\partial t}(\rho Y_i) + \nabla\left(\rho\vec{v}Y_i\right) = -\nabla\vec{J_i} + R_i$	(7)

2.2.2. Combustion Models

The RANS methodology involves subjecting species equations to Reynolds averaging, which results in ambiguous terms for the turbulent scalar flux and the average reaction rate. Turbulent scalar flux modeling calculates the gradient diffusion of gases, and turbulent convection is treated as augmented diffusion. Conversely, the mean reaction rate is modeled using the finite-rate EDC model, which requires precise turbulence prediction. However, the RANS model has limitations, particularly downstream of the air jet, where it shows reduced mixing and reaction rates [28]. In view of the high nonlinearity of reaction rates, the modeling of the mean reaction rate within turbulent flows is considerably challenging and is prone to inaccuracies.

The equilibrium PDF model offers a cost-effective and efficient alternative for simulating RAI flameless combustion [25]. Huang et al. detailed numerical methods for moderate- and low-temperature dilution (MILD) combustion simulations and introduced all-inclusive tabulated chemistry known as the flamelet-generated manifold (FGM) model, which is a sophisticated version of the chemical equilibrium model [29]. They argued that EDC-based models have shortcomings in accurately simulating MILD combustion, whereas the FGM model assures superior and more efficient prediction results [30].

Equilibrium PDF

The chemical equilibrium model for non-premixed combustion was used to simulate flameless combustion. This model simplifies intricate chemical reactions by employing a mixture function (f) and its variance and tabulated chemistry in the form of a PDF, and it can provide detailed chemical composition on the basis of the equilibrium assumption. In cases of intensely turbulent non-premixed combustion, the surface area where fuel and oxygen interact increases significantly, leading to rapid reactions that closely approach chemical equilibrium. Hence, the model is suitable for RAI flameless combustion, in which turbulence is dominant throughout the chamber [25].

In the chemical equilibrium model, it is reasonable to consider the momentary thermochemical condition of the mixture as a function of the instantaneous mixture fraction, expressed in terms of the mass fraction:

$$\mathrm{f} = \frac{Z_i - Z_{i,ox}}{Z_{i,fuel} - Z_{i,ox}} \tag{8a}$$

where Z_i is the mass fraction.

The equation that governs the Favre mean (density-averaged) mixture fraction is

$$\frac{\partial}{\partial t}\left(\rho \overline{f}\right) + \nabla\cdot\left(\rho \vec{v} \overline{f}\right) = \nabla\cdot\left(\frac{\mu_t}{\sigma_t}\nabla \overline{f}\right) + S_m + S_{user} \tag{8b}$$

Apart from providing the Favre mean mixture fraction, the model also solves the conservation equation for the variance of the mixture fraction ($\overline{f'^2}$):

$$\frac{\partial}{\partial t}\left(\rho \overline{f'^2}\right) + \nabla\cdot\left(\rho \vec{v} \overline{f'^2}\right) = \nabla\cdot\left(\frac{\mu_t}{\sigma_t}\nabla \overline{f'^2}\right) + C_g \mu_t \left(\nabla \overline{f}\right)^2 - C_d \rho \frac{\epsilon}{k} \overline{f'^2} + S_{user} \tag{8c}$$

where C_g and C_d are constants with values of 2.86 and 2.0, respectively.

The probability density function, denoted as $p(f)$, can be conceptualized as the proportion of time during which the fluid resides in state f:

$$p(f)\Delta f = \lim_{T\to\infty} \frac{1}{T} \sum_i \tau_i \tag{8d}$$

where T is the time scale (seconds). In practical applications, $p(f)$ is unknown and is modeled using a mathematical function that provides an approximation of experimentally observed PDF shapes.

Composition (Transport) PDF

An alternative approach to Reynolds averaging of the species and energy equations entails formulating a transport equation for their single-point, joint-probability density function (PDF). This PDF, denoted as P, is proportional to the amount of time the fluid occupies specific states of species, temperature, and pressure.

By solving the transport PDF equation, we can efficiently compute various thermochemical moments, such as mean or root-mean-square temperature and mean reaction rate.

The composition PDF model is particularly useful for simulating turbulent non-premixed combustion, where reactions occur in a thin reaction zone [31] and local conditions are rapidly changing. The composition PDF model can efficiently handle statistical variations in temperature, species concentrations, and other properties within the combustion zone.

The composition PDF model employs a statistical description of the reacting mixture, and it involves a joint PDF of the thermodynamic properties and species mass fractions. The joint PDF is a function of the mixture fraction and its variance and serves as a bridge between turbulent fluid flow and chemical reactions. The model can provide detailed information about the chemical composition.

The governing equation for the composition PDF model is

$$\frac{\partial \mathrm{P}(\xi,\zeta;\mathrm{x},\mathrm{t})}{\partial t}+\nabla\cdot(\mathrm{UP}(\xi,\zeta;\mathrm{x},\mathrm{t}))=\nabla\cdot(\Gamma\nabla \mathrm{P}(\xi,\zeta;\mathrm{x},\mathrm{t}))+\mathrm{S}(\xi,\zeta;\mathrm{x},\mathrm{t}) \tag{9}$$

where $\mathrm{P}(\xi, \zeta; \mathrm{x}, \mathrm{t})$ is the joint PDF of the mixture fraction (ξ), ζ is its variance at a spatial location x and time t, U is the mean fluid velocity, and Γ is the diffusion coefficient. The term $\mathrm{S}(\xi, \zeta; \mathrm{x}, \mathrm{t})$ represents the source term, accounting for the effects of turbulent fluctuations, molecular diffusion, and chemical reactions.

By solving the PDF transport equation and using appropriate closure models for the source term, the composition PDF model can capture the complex interactions between turbulence and chemical reactions, providing detailed information about the chemical composition during flameless combustion. This model is particularly useful for simulating non-premixed combustion systems, such as RAI flameless combustion systems, where accurate predictions of the reaction zone and species concentrations are crucial for understanding the combustion process and optimizing performance [32].

2.2.3. Mesh

In CFD analysis, the quality of the mesh plays a crucial role in the accuracy and convergence of simulation results. After inspection, the aspect ratio, skewness, orthogonality, and non-orthogonal angle of the mesh used in the simulation were all maintained within acceptable ranges. The connectivity of the mesh at various hanging nodes, overlapping elements, and gaps between adjacent elements was intact. Furthermore, a mesh independence study based on previous research on a 5 kW RAI flameless combustion simulation indicated that under the premise of an effective grid setting based on flow pattern prediction, controlling the total number of cells in the mesh within the range of 100,000 to 400,000 did not show significant differences in the simulation results for different mesh resolutions [33]. Therefore, the mesh shown in Figure 6 was developed accordingly to have enough cells to generate precise simulation data.

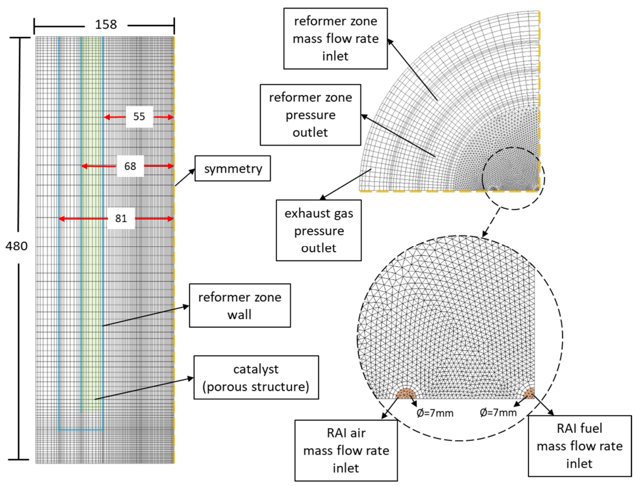

Figure 6. Mesh scale (364,320 cells).

2.2.4. Heat Transfer Efficiency Calculation

The procedure for computing the heat transfer and heat transfer efficiency of the heat exchanger involves the following steps and consideration of water evaporation:

$$\eta = \frac{m\cdot\left[\left(C_{p(water)}\cdot\Delta T_{water}\right) + \left(h_{vaporization}\right) + \left(C_{p(vapor)}\cdot\Delta T_{vapor}\right)\right]}{Q_{fuel}} \tag{10}$$

where Q_{fuel} is the fuel energy feed based on the lower heating value (LHV; kJ/s), m is the mass flow rate of water fed to the reforming zone (kg/s), C_p is the specific heat (kJ/kg K), ΔT_i is the temperature difference between the inlet temperature and the exhaust temperature (K) of material i, and $h_{vaporization}$ is the latent heat of water vaporization (kJ/kg).

2.2.5. Recirculation Ratio Calculation

An important aspect of RAI flameless combustion is the recirculation of internal flue gas through the use of high-speed air jets. A high recirculation ratio leads to a high degree of preheating and extensive dilution of reactants, reducing emissions and preventing the formation of hot spots, thereby significantly improving the efficiency of flameless combustion. Therefore, determining the level of internal flue gas recirculation is necessary to evaluate the performance of flameless combustion [34]. In this study, we calculated the recirculation ratio for five horizontal planes, as shown in Figure 7, through the exported computational results of CFD and Equation (11a), and the flue gas recirculation ratio (Z) for the entire combustion space was obtained through averaging [7,34].

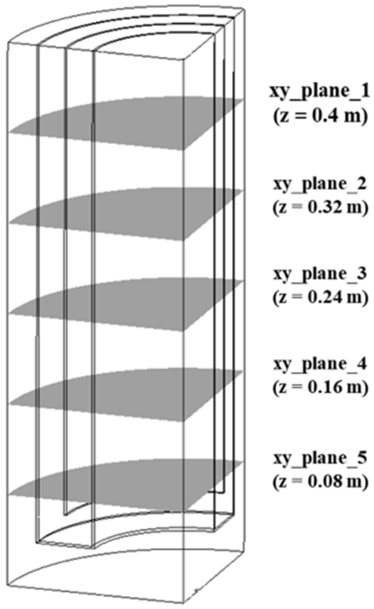

Figure 7. Planes for which the recirculation ratio was calculated.

$$Z = \frac{m_{gas}}{2\left(\dot{m}_{fuel} + \dot{m}_{air}\right)} \tag{11a}$$

where m_{gas} represents the integrated mass flow across a cross-sectional area and is given by

$$\dot{m}_{gas} = \int \rho_{gas}|v_y|\delta A \tag{11b}$$

where $|v_z|$ is the absolute velocity of the combustion gas in the z-axis direction (m/s).

Owing to the presence of a return flow pattern within the combustion chamber, the basic mass flow rate in an xy plane is twice the input flow rate of air $(\dot{m}_{air})$ and fuel $(\dot{m}_{fuel})$.

The recirculation ratio can serve as an indicator of the gas movement's strength, which contributes to the occurrence of flameless combustion.

3. Results and Discussion

3.1. Experimental Results

The experimental results are presented in Table 3. Experiments were conducted thrice for each condition to check the repeatability of temperatures and species concentrations, then averaged. Although theoretical predictions suggest that higher reforming temperatures lead to increased hydrogen production, on the basis of the durability of the experimental equipment and the reduction in thermal NOx emission, the reformer zone outlet temperature (T.C.@3) was controlled at around 700 °C in the experiment. As the heat transfer rate of group C was lower than that of groups A and B, the cooling water flow rate was lower, as shown in Table 1, to set the outlet temperature at around 700 °C.

Table 3. Experimental results. Equivalence ratio: ϕ = 0.8.

		Temperature Distribution					Emission			Heat Transfer	
	Heat Input	**T.C. @1**	**T.C. @2**	**T.C. @3**	**T.C. @4**	**T.C. @5**	**O_2**	**NO_x**	**CO**	**Reformer Zone Heat Transfer**	**Heat Transfer Efficiency**
	(kW)	**(°C)**	**(°C)**	**(°C)**	**(°C)**	**(°C)**	**(%)**	**(ppm)**	**(ppm)**	**(kW)**	**(%)**
Group A—RAI flameless											
A-1	15.4	1005	857	698	460	422	3.3	19	3	12.4	80.5%
A-2	24.6	1025	840	702	504	495		23	6	20.6	83.7%
A-3	33.8	1090	895	722	574	576		33	14	28.4	84.0%
Group B—RAI flameless (with recirculation ring)											
B-1	15.4	975	880	702	458	468	3.3	17	3	12.6	81.8%
B-2	24.6	1000	898	723	482	536		22	7	20.8	84.6%
B-3	33.8	1055	952	717	542	598		33	12	28.5	84.3%
Group C—Flame (premixed burner)											
C-1	15.4	752	1150	687	595	423	3.3	145	9	10.5	68.2%
C-2	24.6	1005	910	696	617	495		79	18	17.9	72.8%
C-3	33.8	1025	925	695	641	535		97	15	25.9	76.6%

Group B, which involved RAI flameless combustion and a recirculation ring, showed the lowest nitrogen oxide emissions, the most uniform temperature, the lowest exhaust gas outlet temperature, and the highest heat transfer efficiency. Group A, with RAI flameless combustion and without a recirculation ring, exhibited a slightly lower heat transfer efficiency than group B; however, the overall combustion performance and heat transfer performance were considerably higher than those of group C. In contrast, group C, representing traditional premixed combustion, produced a large amount of thermal NOx owing to the uneven temperature in the burner front, especially for the low-heat-input case (C-1). However, the experimental results suggest that the porous burner design may enhance the turbulent mixing of fuel and air with increasing burner nozzle velocity, improving the combustion stability and increasing the internal flue gas recirculation rate, which, in turn, reduces thermal NOx emissions [34]. Although C-2 and C-3 had improved combustion quality, their performance was much lower than that of RAI flameless combustion.

Comparing the experimental results within each group, we found that increased heat input did not lead to reduced combustion or reduced heat transfer efficiency; although NO emission increased slightly because of the increased temperature, it was still under the national emission regulation (50 ppm) in the flameless condition and one-third of the emission for the premixed burner. CO emission also increased slightly because of the shortening of the residence time. The air jet velocity can be varied to control the combustion process, as it drives the flue gas recirculation. Further study is required to determine the critical point at which air jet velocity results in incomplete combustion and high thermal NOx emissions and to identify the optimal velocity and recirculation ratio in practical applications and designs of RAI flameless combustion systems [35].

3.2. Simulation Results

3.2.1. Selection and Evaluation of Combustion Models

For the CFD simulation of flameless combustion, the equilibrium PDF model is commonly used as a very economical and fast universal model [25]. However, because this model employs a simplified turbulence–chemistry interaction model, there was a discrepancy between the simulation results and the experimental results for RAI flameless combustion [25]. Therefore, in this section, by comparing equilibrium PDF with the detailed turbulence–chemistry interaction model and composition PDF and by comparing the results of CFD with experimental results, we discuss the appropriate species model with the highest degree of coupling with the experimental results and its advantages and disadvantages.

Table 4 presents a comparison of experimental results with the CFD of both models for group A. After noting that composition PDF showed better agreement with the group A experiments, the center case of group B (B-2) was examined to check its repeatability. The comparison temperature of CFD was calculated by surface averaging at the same level of the experimental position to eliminate the temperature deviation caused by overly precise temperature extraction in the CFD simulation compared with the actual experiment's thermocouples. The data showed that most of the results of the composition PDF model were closer to experimental results compared with the extent of agreement between the equilibrium PDF model's results and experimental results. However, the computational time was more than 10 times longer.

Table 4. Comparison of results of different models used in CFD and experimental results (including the iteration speed and total number of iterations).

Group	Species Model	T.C.@1	T.C.@2	T.C.@3	T.C.@4	T.C.@5	Emission		Computational Speed	Total Iteration Steps for Convergence
		Top	Bottom	Catalyst	Gas	Wall	NO_x	CO		
		(K)	(K)	(K)	(K)	(K)	(ppm)	(ppm)	[s/Iteration]	(Iteration)
A-1	Experimental data	1278	1130	971	733	695	19	3	-	-
	E-PDF	1545	1488	1035	1011	998	33.6	14.4	3.3	38,445
	C-PDF	1352	1359	1013	814	859	8.5	19.2	46.2	16,959
A-2	Experimental data	1298	1113	975	777	768	23	6	-	-
	E-PDF	1605	1508	961	1229	1075	47.4	15.8	2.3	39,454
	C-PDF	1389	1486	965	1017	891	33.1	16.7	47.5	24,956
A-3	Experimental data	1363	1168	995	847	849	37	22	-	-
	E-PDF	1788	1655	1034	1437	1250	89.5	23.9	2.3	60,652
	C-PDF	1496	1513	955	1221	1019	97.5	18.5	55.7	19,775
B-2	Experimental data	1273	1171	996	755	809	22	7	-	-
	E-PDF	1657	1588	1032	954	923	57.5	23.8	3.5	55,482
	C-PDF	1634	1552	1057	907	833	21.3	17.9	47.9	17,757

From the bar graph comparison in Figure 8, it can be intuitively observed that for RAI flameless combustion, the composition PDF model showed a higher degree of fit with the experimental results in terms of the temperature and outlet emissions. However, with an increase in the heat input, the deviation between the CFD results and the experimental results increased slightly, probably because of the inaccurate setting of the heat loss value in the CFD simulation, which should be improved in the future.

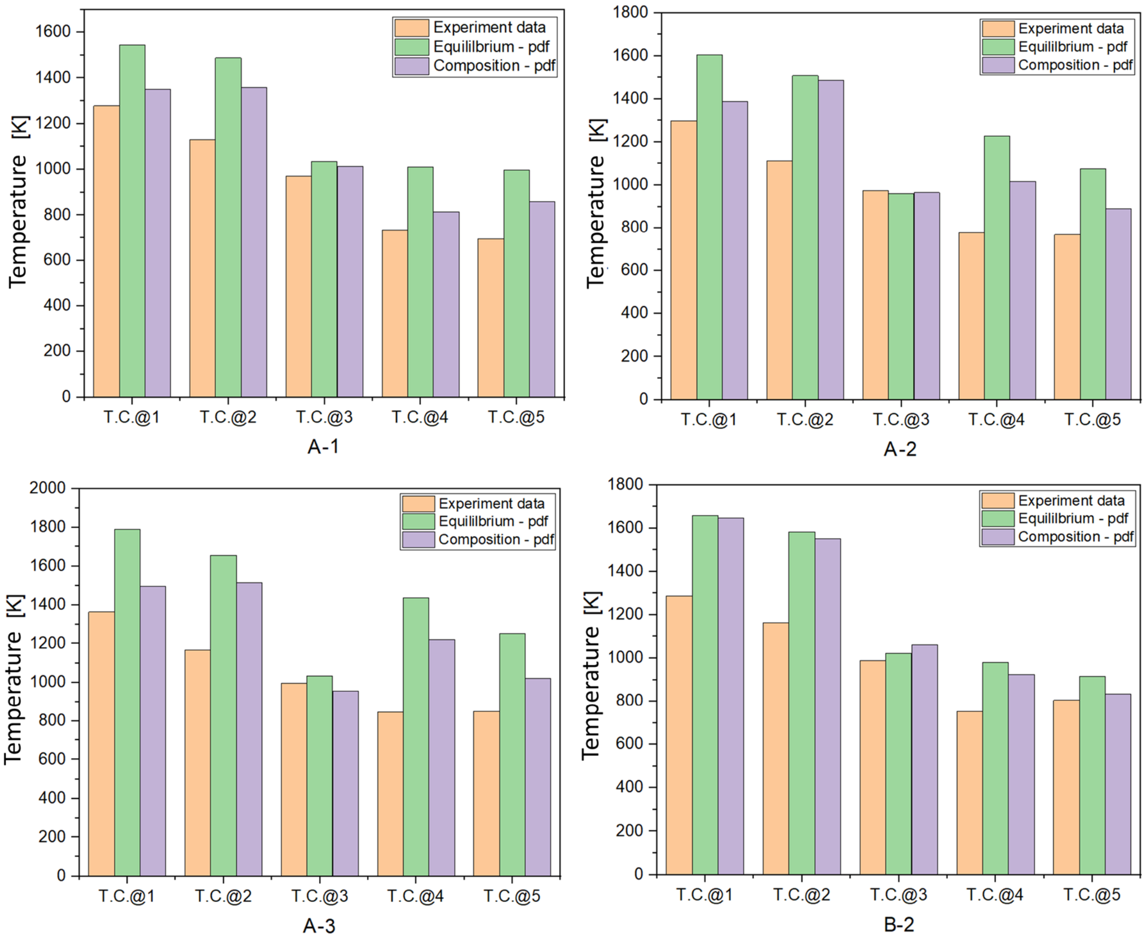

Figure 8. Evaluation of fit between different models used in CFD and experimental results.

Figure 9 shows the internal temperature distribution for A-2 and B-2 for the equilibrium PDF and composition PDF models, and Figure 10 shows the wall heat transfer coefficient in the reforming region. Overall, the equilibrium PDF model showed a broader temperature distribution than the composition PDF model, especially at the top area of the combustion chamber, indicating higher diffusion of species and their chemical reactions. In comparison, the composition PDF model showed more uniform temperature, which resulted in a higher heat transfer rate to the reformer and a lower temperature at the exhaust of the combustion chamber.

The results showed that the composition PDF model's results were closer to the experimental results than those of the equilibrium PDF model, and the former model showed a higher overall heat transfer efficiency and a more uniform temperature distribution. This might be due to the composition PDF model capturing the statistical distributions of material concentration and temperature under turbulence more accurately than the equilibrium PDF and EDC models, thereby providing a more precise representation of turbulent–chemical interactions [36]. Furthermore, the composition PDF model solves the transport equation for the joint-probability density function of material concentration and temperature, which is helpful in reducing numerical diffusion, which is frequently observed in the EDC and equilibrium PDF models. Therefore, the model predicts pollutant emissions and the flame structure more accurately [37].

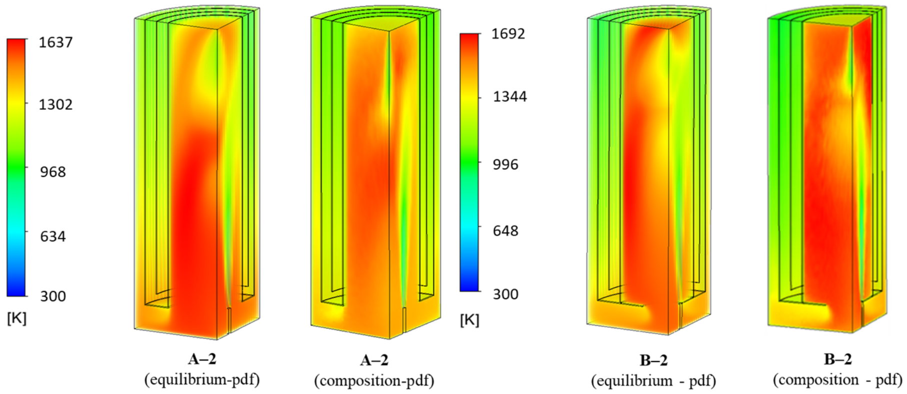

Figure 9. Comparison of temperature contours of the combustion zone.

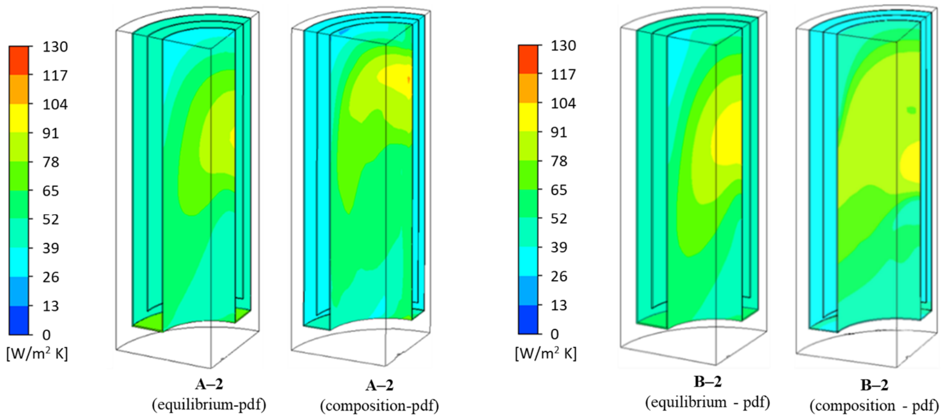

Figure 10. Comparison of heat transfer coefficient contours on the inner wall of the reforming zone.

The composition PDF model is applicable to various combustion states, including premixed, non-premixed, and partially premixed flames, making it highly suitable for RAI flameless combustion simulations that involve different fuel and oxidizer injection strategies [38]. However, it is noteworthy that, as shown in Table 4, because of the higher complexity involved with the detailed chemistry and solving of PDF transport equations, the composition PDF model requires a significantly longer iteration time than the EDC and equilibrium PDF models. The choice between these models depends on the specific problem, required accuracy, and available computational resources.

3.2.2. Effect of Recirculation Ring on RAI Flameless Combustion

In the design of a cylindrical hydrogen reformer with RAI flameless combustion, a recirculation ring was incorporated in the combustion zone for group B. This design modification was aimed at increasing the recirculation of flue gas in the combustion area, thereby promoting more thorough reactions of species, which consequently enhanced the heat transfer efficiency of the reformer [39]. This section discusses the use of a faster and more economical equilibrium PDF model for CFD analysis to relatively evaluate and analyze the effects of introducing a recirculation ring and to determine its mechanisms [40].

As shown in Figure 11, the presence or absence of a recirculation ring did not significantly influence the fluid flow and vertical velocity (z-vel) in the combustion zone. However, as indicated by the results shown in Figure 12, the concentration of hydroxyl (-OH) radicals in the combustion area showed an overall upward and increasing trend within the combustion zone. The increasing concentration of OH radicals implies increased reactivity in the combustion zone, especially near the reformer wall. Concurrently, as shown in Figure 13, the position of the H_2 (active intermediate fuel species) contour shifted upward of the combustion chamber, signifying more uniform temperature distribution in the combustion chamber, as shown in Figure 8 and as similarly depicted by the OH radical (signifying active reaction zone) in Figure 12 [41,42]. This is likely to contribute to higher heat transfer efficiency and more uniform temperature when a recirculation ring is used, as shown in Figures 8 and 9.

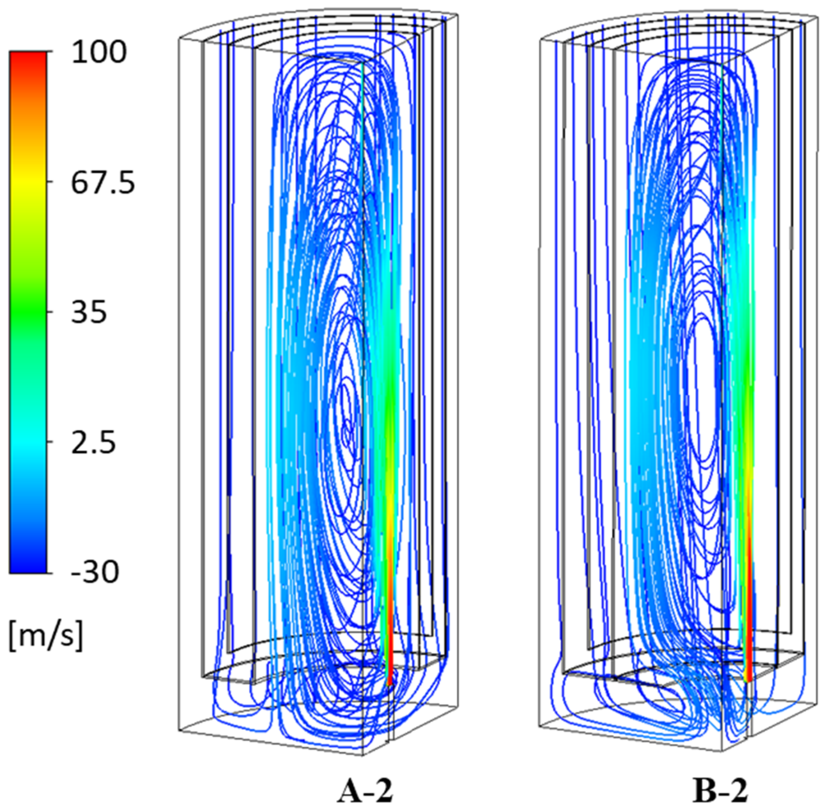

Figure 11. Fluid streamline (color indicates velocity).

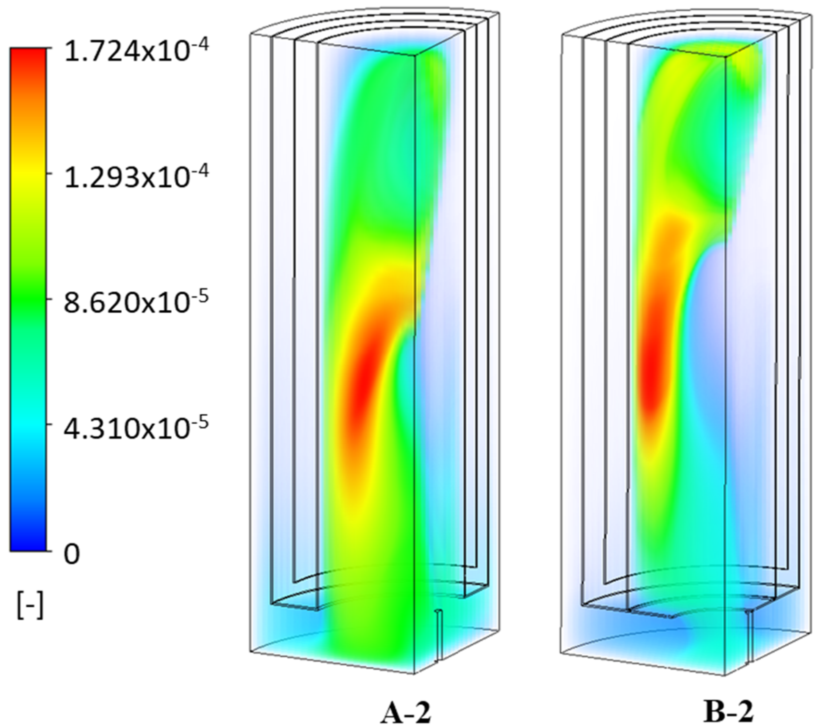

Figure 12. OH radical concentration in the combustion zone.

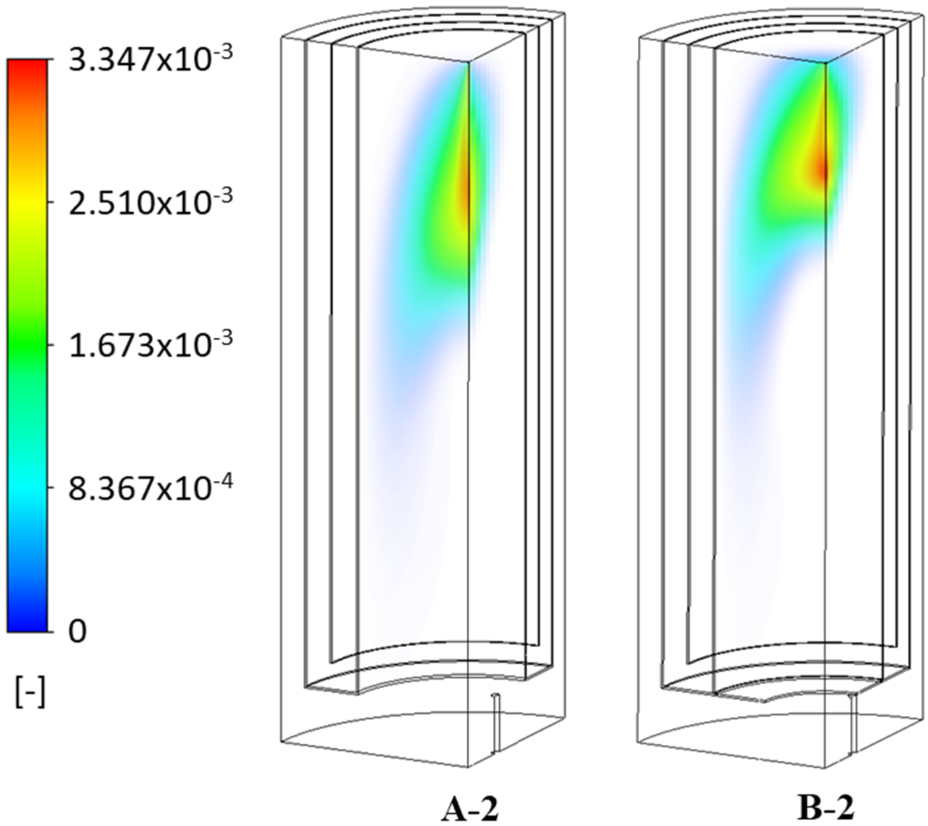

Figure 13. H_2 concentration in the combustion zone.

3.2.3. Difference between RAI Flameless and Premixed Burners

In this section, we present a comparison of simulation results between A-2, which involved RAI flameless combustion, and C-2, which employed traditional premixed combustion. The composition PDF model, which is the most accurate according to experimental results, was chosen for group A-2, and the EDC model, which is commonly used for premixed combustion, was chosen for group C-2.

As evidenced by the comparison shown in Figure 14, CFD simulation results suggest that flameless combustion leads to more rapid and more complete consumption of oxygen. The difference in oxygen concentration within the combustion chamber primarily stems from the distinct combustion mechanisms of the two models. Flameless combustion is a high-temperature, low-oxygen, diffusion-controlled process, which implies that the fuel and oxygen do not mix thoroughly before being burnt; instead, they undergo combustion and oxidize in the diffusion layer. This mode of combustion is characterized by significant gradients in fuel and oxygen concentrations, leading to rapid oxygen depletion. Furthermore, the uniform temperature and low-oxygen conditions in flameless combustion reduce the amount of some combustion byproducts (e.g., NOx) [43].

Figure 15 shows the difference in high-temperature regions (above 1400 K) within the combustion chamber. Clearly, for given heat input, the high-temperature zone is significantly reduced for the RAI flameless burner compared with the premixed burner. This is because of the absence of a distinct flame front, which is observed in traditional combustion. Furthermore, the high recirculation of gas flow increases mixing, as well as heat transfer, which reduces the hot temperature zone because of the low reaction rate and increased heat transfer to the reformer zone. This leads to a reduction in the production of harmful byproducts (NOx) and simultaneously improves the energy efficiency.

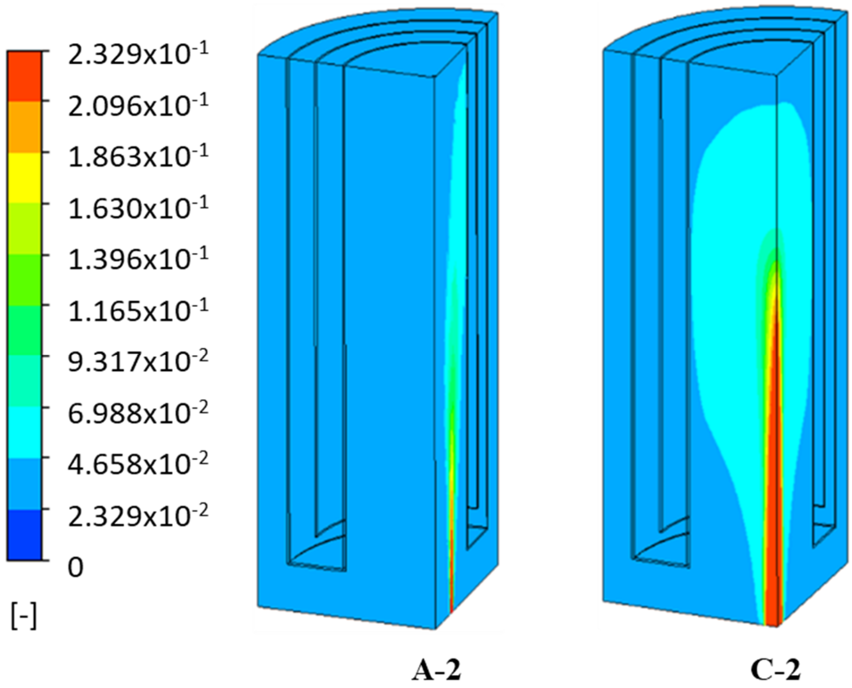

Figure 14. Oxygen consumption diagram for the combustion zone.

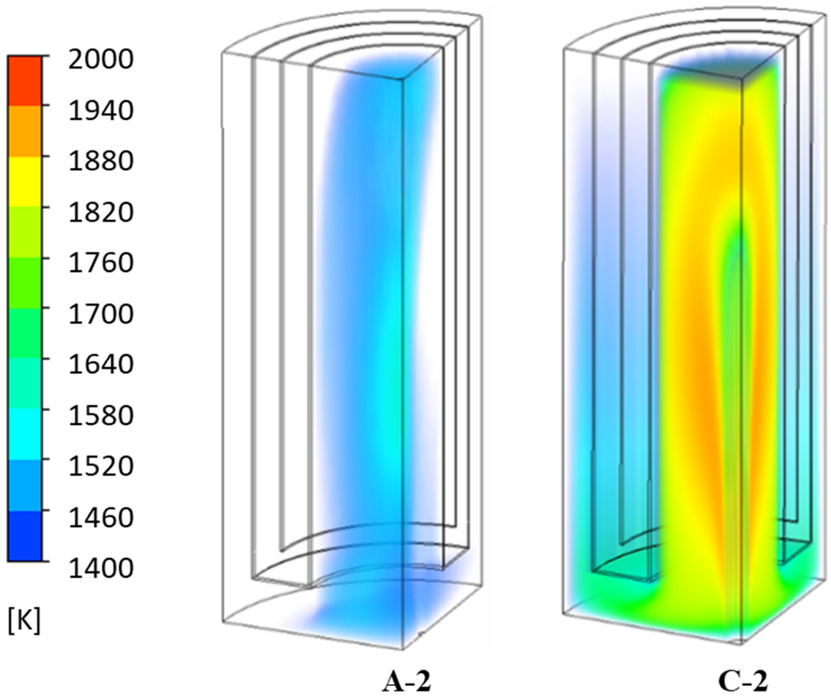

Figure 15. Schematic diagram of a high-temperature zone (>1400 K).

Figure 16 shows the magnitude of the vertical downward velocity in the combustion chamber. Evidently, owing to the high-speed jet air, RAI shows a very strong convection phenomenon in the near-wall area. This strong convection enhances heat transfer between the combustion region and the reforming region, leading to the difference in the wall heat transfer coefficients shown in Figure 17.

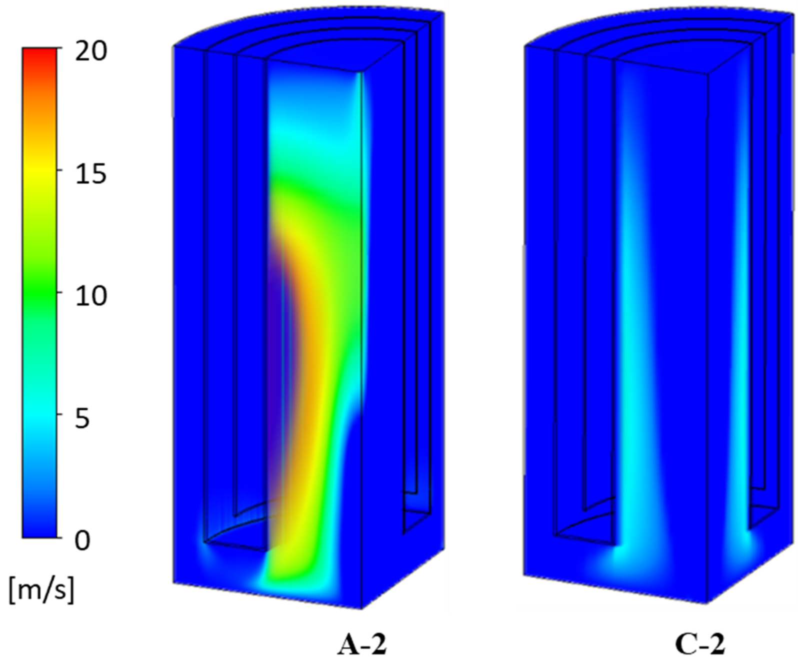

Figure 16. Schematic diagram of the vertical downward velocity in the combustion zone.

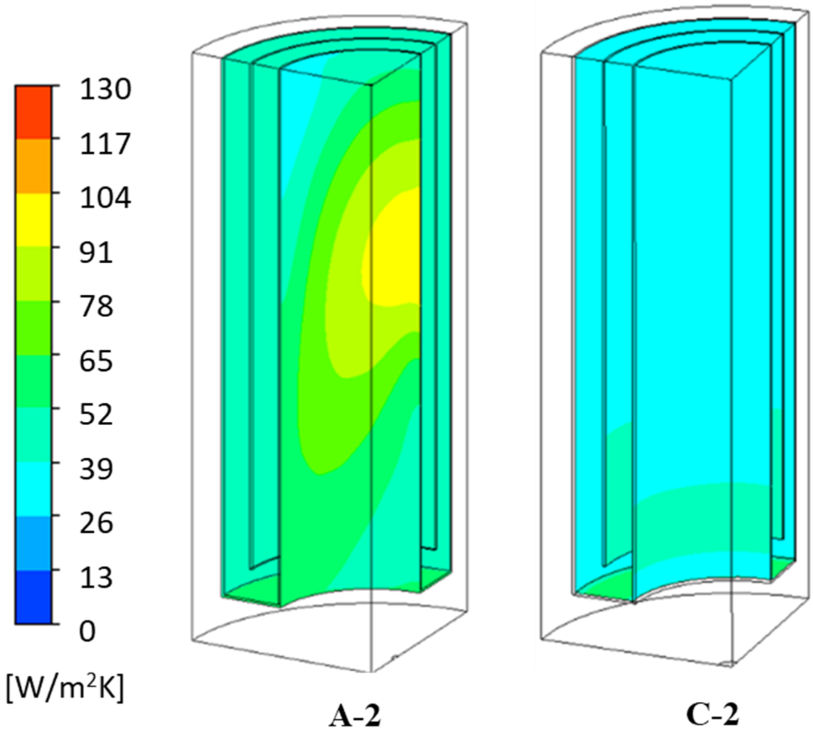

Figure 17. Schematic diagram of the surface heat transfer coefficient.

3.2.4. Flue Gas Recirculation Characteristics

Table 5 presents the recirculation rate in the combustion chamber obtained from simulation results. The configuration's xy_plane_5 located at the bottom showed the highest recirculation rate, whereas xy_plane_1 located at the top exhibited the lowest value because of the limited penetration of the air jet. There is a stark fivefold difference in the recirculation ratio between the flameless group (A and B) and the conventional burner (C). The recirculation rate is closely associated with the heat transfer efficiency. A higher recirculation rate leads to considerable preheating and dilution of the reactants, as well as increased flow velocity near the wall. This can significantly enhance the overall combustion efficiency and reduce emissions and the heat and mass transfer rate, thereby preventing the formation of hot spots and reducing the risk of nitrogen oxide (NOx) formation. Group B showed the highest recirculation rate, which is the reason for the highest heat transfer coefficient and low NO emission in the experimental results.

Table 5. Results of recirculation ratio calculation.

	Recirculation Ratio of Each Plane					Space Average Recirculation Ratio
	xy_Plane_1	xy_Plane_2	xy_Plane_3	xy_Plane_4	xy_Plane_5	
Group A—Flameless						
A-1	0.26	1.73	5.17	6.92	9.77	4.77
A-2	0.28	1.77	5.21	6.88	9.75	4.78
A-3	0.29	1.80	5.21	6.79	9.68	4.61
Group B—Flameless (recirculation ring)						
B-1	1.15	2.16	5.54	7.26	9.55	5.13
B-2	1.14	2.21	5.63	7.25	9.55	5.16
B-3	1.12	2.28	5.66	7.21	9.56	5.17
Group C—Flame (premixed)						
C-1	0.02	0.37	1.02	1.33	1.85	0.92
C-2	0.04	0.37	1.03	1.38	2.03	0.97
C-3	0.04	0.38	1.01	1.38	2.01	0.96

4. Conclusions

This study provides design ideas for the enhancement of the heat transfer performance of a cylindrical reformer with RAI flameless combustion on the basis of experimental and simulation results. Experimental results showed that RAI flameless combustion could enhance the heat transfer efficiency, resulting in expansion of the cylindrical design of the reformer to a higher capacity. Compared with a premixed burner, RAI flameless combustion improved the heat transfer efficiency by up to 20%. CFD simulation results supported the experimental results and indicated the detailed mechanism of heat transfer enhancement. Uniform high temperature and high flow velocity near the heat exchanger surface were the most distinguished features of RAI flameless combustion. Uniform low oxygen concentration was also caused by highly recirculating flow, realizing flameless combustion. The recirculation ratio calculated from CFD results showed that the RAI flameless combustion had fivefold higher recirculation compared with the premixed burner. Installing a recirculation ring at the exit of the combustion chamber influenced the flow pattern in the case of RAI flameless combustion by increasing the recirculation ratio by about 8%, which resulted in a higher heat transfer coefficient.

Despite showing good agreement with experimental results, the combustion model of turbulence interaction requires further study. The effect of turbulence is reflected in the EDC model, but the correctness of the turbulence model, which employs two equations, is not sufficient to simulate flameless combustion accurately. A high-speed air jet and induced high-turbulence flow recirculation can be assumed to provide the required turbulent intensity for combustion. Therefore, reaction kinetics represent the most important parameter controlling flameless combustion, which is why the composition PDF model showed the best fitting performance among the three tested models. However, owing to its long iteration time, the equilibrium PDF model can be used as an alternative model to economically generate reasonable initial data for RAI flameless combustion.

The findings from this study are expected to contribute to a broader understanding of the heat transfer mechanism of RAI flameless combustion, and they show the feasibility of the application of this type of combustion to the design of commercial reformers to produce hydrogen. The incorporation of a recirculation ring in the combustion area to improve heat transfer efficiency in a hydrogen reformer is promising, and it should be explored further in future research.

Author Contributions: Conceptualization, D.S.; methodology, D.S.; resources, D.S.; data curation, R.Z.; writing—original draft preparation, R.Z.; writing—review and editing, R.Z.; visualization, R.Z.; supervision, D.S.; project administration, D.S.; funding acquisition, D.S. All authors have read and agreed to the published version of the manuscript.

Funding: This research was funded by KETEP (Korea Institute of Energy Technology Evaluation and Planning; No. 202003040030090) and KEIT (Korea Evaluation Institute of Industrial Technology; No. 20213030040550).

Conflicts of Interest: The authors declare no conflict of interest.

Nomenclature

E_{ij} is a component of the rate of deformation; $\vec{F}$ contains other model-dependent source terms (porous media and user-defined sources); H is the enthalpy (kJ/kg); I is the radiation intensity (W/sr); k_t is the turbulent thermal conductivity; n is the refraction coefficient; p is the static pressure (momentum conservation equations) (Pa); $\vec{r}$ is the position vector; $\vec{s}'$ is the scattering direction; $\vec{s}$ is the direction vector; S_h includes the heat of chemical reaction and any other volumetric heat sources (kJ); T is the local temperature (discrete-ordinates (DO) radiation model) (K); u_i is the velocity component in the i direction (m/s); Y_i^* is the fine-scale species mass fraction after the reaction progresses for time τ^*.

References

1. Crabtree, G.W.; Dresselhaus, M.S.; Buchanan, M.V. The Hydrogen Economy. *Phys. Today* **2004**, *57*, 39–44. [CrossRef]
2. Singhal, S.C. Solid oxide fuel cells for stationary, mobile, and military applications. *Solid State Ion.* **2002**, *152–153*, 405–410. [CrossRef]
3. Ni, M.; Leung, M.K.H.; Leung, D.Y.C. Technological development of hydrogen production by steam reforming of methane. *Renew. Sustain. Energy Rev.* **2007**, *11*, 827–853.
4. Goyal, H.O.; Ghose, M.K. Hydrogen production by steam reforming of ethanol for PEM fuel cells. *Int. J. Hydrogen Energy* **2001**, *26*, 923–929.
5. Rostrup, J.R.; Christiansen, L.J. *Concepts in Syngas Manufacture*; Imperial College Press: London, UK, 2011.
6. Ahmed, S.; Krumpelt, M. Hydrogen from hydrocarbon fuels for fuel cells. *Int. J. Hydrogen Energy* **2001**, *26*, 291–301. [CrossRef]
7. Kim, B.; Shin, D. A study on the heat flow characteristics in a flameless combustion furnace with a reverse air injection method installed with a double tube heat exchanger. *Trans. Korean Soc. Mech. Eng.* **2020**, *44*, 219–230. [CrossRef]
8. Shin, T.; Shin, D. Study on the Operation Range and Performance of Reverse Air Injection Flameless Combustion Depending on LPG Flow Rate and Air Injection Velocity. *Trans. Korean Soc. Mech. Eng.* **2021**, *45*, 541–548. [CrossRef]
9. Shin, J.S.; Shin, D. Study on Emission Characteristics Based on the Fuel Flow Rate and Stoichiometric Ratio of a Swirling Flameless Furnace. *Trans. Korean Soc. Mech. Eng.* **2021**, *45*, 559–568. [CrossRef]
10. Hussain, T.; Kaviany, M. Flameless combustion of gaseous fuel with air preheated by recirculation of combustion products. *Combust. Flame* **2011**, *158*, 642–650.
11. Hosseini, S.E.; Wahid, M.A. Enhancement of exergy efficiency in combustion systems using flameless mode. *Energy Convers. Manag.* **2014**, *86*, 1154–1163. [CrossRef]
12. Chinnici, A.; Tian, Z.F.; Lim, J.H.; Nathan, G.J.; Dally, B.B. Comparison of system performance in a hybrid solar receiver combustor operating with MILD and conventional combustion. *Sol. Energy* **2017**, *147*, 479–488. [CrossRef]
13. Kilian, C.A. *Numerical Simulation of Non-Premixed Laminar and Turbulent Flames by Means of Flamelet Modelling Approaches*; Universitat Politècnica de Catalunya: Barcelona, Spain, 2005; ISBN 8468917435.
14. Launder, B.E.; Spalding, D.B. The numerical computation of turbulent flows. *Comput. Methods Appl. Mech. Eng.* **1974**, *3*, 269–289. [CrossRef]
15. Modest, M.F. *Radiative Heat Transfer*; Elsevier: Amsterdam, The Netherlands, 2003.
16. Pope, S.B. Computationally efficient implementation of combustion chemistry using in situ adaptive tabulation. *Combust. Theory Model.* **1997**, *1*, 41–63. [CrossRef]
17. Lacaze, G.; Oefelein, J.C. A fully coupled, high fidelity simulation of a turbulent mixing and combustion experiment. *Proc. Combust. Inst.* **2012**, *34*, 1353–1360.
18. Peters, N. *Turbulent Combustion*; Cambridge University Press: Cambridge, UK, 2000.

19. Smith, P.J.; Shen, C.K. Turbulent premixed combustion in V-shaped flames: Experiments and a composition pdf model. *Combust. Flame* **1998**, *115*, 528–542.
20. Reitz, R.D.; Bracco, F.V. Mechanisms of atomization of a liquid jet. *Phys. Fluids* **1982**, *25*, 1730–1742. [CrossRef]
21. Fox, R.O. *Computational Models for Turbulent Reacting Flows*; Cambridge University Press: Cambridge, UK, 2003.
22. Llorca, J.; Homs, N.; Sales, J.; de la Piscina, P.R. Ethanol steam reforming on Rh/CeO_2 catalysts: The role of ceria as a promoter. *J. Catal.* **2002**, *209*, 306–317. [CrossRef]
23. Fatsikostas, A.N.; Verykios, X.E. Steam reforming of ethanol for the production of hydrogen for fuel cell applications. *Int. J. Hydrogen Energy* **2004**, *29*, 1555–1560.
24. Pacheco, M.A.; Marshall, C.L. Review of dimethyl ether as an energy source. *J. Power Sources* **1997**, *65*, 193–204.
25. Zhu, R.; Shin, D. Heat transfer characteristics of tubular heat exchanger using reversed air injection flameless combustion. *Appl. Therm. Eng.* **2023**, *230 Pt B*, 120713.
26. Galletti, C.; Ferrarotti, M.; Parente, A.; Tognottia, L. Reduced NO formation models for CFD simulations of MILD combustion. *Int. J. Hydrogen Energy* **2015**, *40*, 4884–4897. [CrossRef]
27. Raithby, G.D.; Chui, E.H. A finite-volume method for predicting a radiant heat transfer in enclosures with participating media. *J. Heat Transf.* **1990**, *112*, 415–423. [CrossRef]
28. Lupant, D.; Lybaert, P. Assessment of the EDC combustion model in MILD conditions with in-furnace experimental data. *Appl. Therm. Eng.* **2015**, *75*, 93–102. [CrossRef]
29. He, D.; Yu, Y.; Kuang, Y.; Wang, C. Analysis of EDC constants for predictions of methane MILD combustion. *Fuel* **2022**, *324*, 124542. [CrossRef]
30. Huang, X.; Tummers, M.J.; van Veen, E.H.; Roekaerts, D.J.E.M. Modelling of MILD combustion in a lab-scale furnace with an extended FGM model including turbulence and radiation interaction. *Combust. Flame* **2022**, *237*, 111634. [CrossRef]
31. Pope, S.B. PDF methods for turbulent reactive flows. *Prog. Energy Combust. Sci.* **1985**, *11*, 119–192. [CrossRef]
32. Huang, Y.; Sung, H.J.; Hwang, W. Assessment of presumed probability density function and flamelet models in simulating nonpremixed turbulent CO/H_2 jet flames. *Combust. Flame* **2004**, *139*, 222–240.
33. Smagorinsky, J. General circulation experiments with the primitive equations. *Mon. Weather Rev.* **1963**, *91*, 99–164. [CrossRef]
34. Li, P.; Mi, J.; Wang, F. Effects of equivalence ratio and reactant mixing mode on flameless combustion. *Chin. J. Electr. Eng.* **2011**, *31*, 20–27.
35. Ruan, L.; Chen, Y.; Zhu, X. Effects of jet speed and recirculation ratio on heat transfer characteristics in a porous media burner. *Energy Convers. Manag.* **2019**, *196*, 1179–1188.
36. Yang, W.; Blasiak, W. Large eddy simulation of turbulent combustion in a bluff-body burner with internal exhaust gas recirculation. *Fuel* **2006**, *85*, 2135–2144.
37. Ruppert, A.M.; Weinberg, K.; Emig, G. Steam reforming and oxidative steam reforming of ethanol: The first step in the exploitation of bioethanol in fuel cells. *ChemSusChem* **2009**, *2*, 807–810.
38. Da Silva, A.A.R.; Noronha, F.B.; Souza, M.J.B.; Schmal, M. Hydrogen from ethanol: Review of production technologies. *J. Power Sources* **2019**, *423*, 130–143.
39. Rossetti, I. Testing of different catalysts for steam reforming of ethanol at low temperature. *Int. J. Hydrogen Energy* **2008**, *33*, 6351–6359.
40. Pantoleontos, G.; Kondarides, D.I.; Verykios, X.E. Ethanol Steam Reforming for Hydrogen Generation over Noble Metal Catalysts. *Appl. Catal. B Environ.* **2015**, *170–171*, 107–121.
41. Adam, P.S.; Andrew, E.L. Exergy analysis of hydrogen production via steam methane reforming. *Int. J. Hydrogen Energy* **2007**, *32*, 4811–4820.
42. Haworth, D.C. Progress in probability density function methods for turbulent reacting flows. *Prog. Energy Combust. Sci.* **2010**, *36*, 168–259. [CrossRef]
43. Hawkes, E.; Sankaran, R.; Sutherland, J.C.; Chen, J.H. Direct numerical simulation of turbulent combustion: Fundamental insights towards predictive models. *J. Phys.* **2005**, *16*, 26–30. [CrossRef]